VTT Technical Research Centre of Finland

Computation of the incompressible viscous -flow around a tractor thruster using a sliding-mesh technique

Sanchez-Caja, Antonio; Rautaheimo, Patrik; Salminen, Esa; Siikonen, Timo

Published in:
Proceedings of 7th International Conference on Numerical Ship Hydrodynamics

Published: 01/01/1999

Document Version
Publisher's final version

COMPUTATION OF THE INCOMPRESSIBLE VISCOUS FLOW AROUND A TRACTOR THRUSTER USING A SLIDING-MESH TECHNIQUE

Antonio Sánchez-Caja[1], Patrik Rautaheimo[2], Esa Salminen[2] and Timo Siikonen[2]
[1] VTT Manufacturing Technology, Maritime and Mechanical Engineering
P.O.Box 1705, FIN-02044 VTT, Finland
Fax: 358-9-456 0619; E-Mail: Antonio.Sanchez@vtt.fi
[2] Helsinki University of Technology, Laboratory of Applied Thermodynamics
P.O.Box 4400, FIN-02015 HUT, Finland
Fax: 358-9-451 3418; E-Mail: Patrik.Rautaheimo@hut.fi,
Esa.Salminen@hut.fi, Timo.Siikonen@hut.fi

ABSTRACT

The unsteady flow around a tractor thruster is simulated by solving the RANS equations with a sliding mesh technique. A multiblock Navier–Stokes solver (FINFLO) developed at Helsinki University of Technology is used in the calculations. In this paper a computational method with special emphasis on the sliding mesh technique is described. The flow over a BB series propeller is analysed and a comparison with experimental data is made. This calculation is made with a fine grid and used as a reference for the rest of the computations, where the flow around the tractor thruster is simulated. The thruster consists of the BB-series propeller, a pod and a strut. The sliding surface is located between the propeller and strut. The calculations are performed in two different ways. In the first case the flow quantities are circumferentially averaged on the sliding surface in order to reduce computing time. The second calculation is time-accurate.

INTRODUCTION

Azimuthing propulsor systems have long been confined to low propulsive power levels. The reason is the limitation of torsional moments that can be transmitted by Z-drive units. Podded propulsors have removed such a limitation. An electric motor coupled directly to the propeller is housed inside a pod and located as a separated unit outside the ship hull. Podded propulsors have many advantages over conventional ones, e.g. improved wake to the propeller, and, consequently, reduction of vibrations and noise, better manoeuvrability, simpler engine control and more flexibility for the selection of ship forms in the hydrodynamic design of the stern. This also allows space savings as well as higher propulsion efficiency. Over the last decade Kvaener Masa-Yards and ABB have pioneered the use of this innovative Diesel-electric propulsion system for high propulsive power levels. They have named it Azipod (azimuthing podded drive).

In recent years Reynolds Average Navier–Stokes (RANS) solvers have been increasingly applied at several research institutions around the world for the prediction of the flow around marine propeller blades. At the Technical Research Centre of Finland (VTT) the application of RANS solvers to marine propeller analysis started in 1995 with encouragingly good results [1]. Since then the application of RANS solvers have been extended to more complex propeller configurations, e.g. to podded propulsors. In such complicated geometries the flow is basically unsteady, which should be taken into account in the computational model.

There are different approaches to solving the Navier–Stokes equations in the case of rotating machinery. The most accurate and straightforward one is to divide the computational mesh into stationary blocks fixed to the non-rotating part of the machinery and into rotating blocks. They are connected to each other through a sliding surface. The problem with this approach is that the flow is modelled as being time dependent, which requires a great deal of computing time. Another and cheaper method is to find a steady-state solution in a rotating coordinate system. Then the velocities are expressed in the rotating frame and extra Coriolis and centrifugal forces are introduced into the Navier–Stokes equations. A disadvantage of this approach is that there might be numerical problems far away from the rotating axis, and also for turbulence modelling one must keep in mind what velocities should be used to define the strain and vorticity rates. An alternative approach is to use the absolute Cartesian velocities in the rotating frame. This method is accurate only with axisymmetric flows, but is applied in the present study for the

unsteady flow around the Azipod, and compared to the time-accurate calculation with the sliding mesh.

The multiblock Navier-Stokes solver (FINFLO) used in this study has been developed at Helsinki University of Technology [2]. The original code has been extended for incompressible flows using a pseudo-compressibility method [3]. In the following, the physical modelling and the solution methods used are described. Next, the steady-state analysis of a BB series propeller is provided, and the results are compared with experimental data. This calculation is made with a very fine grid to serve as a reference for the rest of the computations. A quasi-steady analysis is then performed for the tractor thruster using circumferentially averaged conditions on the sliding surface. The thruster consists of the above mentioned BB-series propeller, a pod and a strut. The final calculation for the thruster is time-accurate and the sliding-mesh technique is applied. Comparison between the calculated and the mean experimental thrust and torque forces is provided, and some details of the flow are illustrated. The validation presented in this paper has been possible thanks to the release of some experimental data from some of the first preliminary versions of the Azipod system.

SOLUTION METHODS

Governing Equations

The flow simulation is based on the solution of the Reynolds averaged Navier–Stokes equations in a coordinate system which rotates around the x-axis with an angular velocity Ω. Turbulence is modelled using the $k-\epsilon$-model. The rotational speed of the domain is $\vec{\Omega}\times\vec{r} = [0, -\Omega z, \Omega y]^T$. The equations can be written in a conservative form without the energy equation as

$$\frac{\partial U}{\partial t} + \frac{\partial (F-F_v)}{\partial x} + \frac{\partial (G-G_v)}{\partial y} + \frac{\partial (H-H_v)}{\partial z} = Q \tag{1}$$

where U is a vector of conservative variables $U = [\rho,\ \rho u,\ \rho v,\ \rho w,\ \rho k,\ \rho\epsilon]^T$, ρ is the density, u, v and w are the absolute velocity components in a Cartesian coordinate system, and Q is a source term. In the steady-state solution the time-derivative term is meaningless and is only utilized in the numerical solution. Instead, a source term is introduced in the momentum equation [4]. Altogether with the turbulence equations, the source term becomes $Q = [0, 0, \rho\Omega w, -\rho\Omega v, Q_k, Q_\epsilon]^T$. Thus in the quasi-steady simulation the source term Q has non-zero components for the equations for y- and z-momentum and turbulence. In the time-accurate integration the source terms for the turbulence equations are retained, but there are no source terms in the momentum equation and the time-derivative must be discretized accurately. However, the differences in these two simulation approaches are small.

The inviscid fluxes are

$$F = \begin{pmatrix} \rho\hat{u} \\ \rho u\hat{u} + p + \frac{2}{3}\rho k \\ \rho v\hat{u} \\ \rho w\hat{u} \\ \rho\hat{u}k \\ \rho\hat{u}\epsilon \end{pmatrix} \quad G = \begin{pmatrix} \rho\hat{v} \\ \rho u\hat{v} \\ \rho v\hat{v} + p + \frac{2}{3}\rho k \\ \rho w\hat{v} \\ \rho\hat{v}k \\ \rho\hat{v}\epsilon \end{pmatrix}$$

$$H = \begin{pmatrix} \rho\hat{w} \\ \rho u\hat{w} \\ \rho v\hat{w} \\ \rho w\hat{w} + p + \frac{2}{3}\rho k \\ \rho\hat{w}k \\ \rho\hat{w}\epsilon \end{pmatrix} \tag{2}$$

where p is the pressure. The kinetic energy of turbulence $2/3\rho k$ is connected with the pressure and appears here in the convective, i.e. inviscid fluxes. Above the convective, i.e. the relative speeds are

$$\hat{u}_i = u_i - \left(\vec{\Omega}\times\vec{r}\right)_i \tag{3}$$

In this case the individual components are

$$\begin{aligned} \hat{u} &= u \\ \hat{v} &= v + \Omega z \\ \hat{w} &= w - \Omega y \end{aligned} \tag{4}$$

The viscous fluxes are

$$F_v = \begin{pmatrix} 0 \\ \tau_{xx} + \frac{2}{3}\rho k \\ \tau_{xy} \\ \tau_{xz} \\ \mu_k(\partial k/\partial x) \\ \mu_\epsilon(\partial\epsilon/\partial x) \end{pmatrix}$$

$$G_v = \begin{pmatrix} 0 \\ \tau_{xy} \\ \tau_{yy} + \frac{2}{3}\rho k \\ \tau_{yz} \\ \mu_k(\partial k/\partial y) \\ \mu_\epsilon(\partial\epsilon/\partial y) \end{pmatrix} \tag{5}$$

$$H_v = \begin{pmatrix} 0 \\ \tau_{xz} \\ \tau_{yz} \\ \tau_{zz} + \frac{2}{3}\rho k \\ \mu_k(\partial k/\partial z) \\ \mu_\epsilon(\partial\epsilon/\partial z) \end{pmatrix}$$

where the viscous stress tensor is

$$\tau_{ij} = \mu\left[\frac{\partial u_j}{\partial x_i} + \frac{\partial u_i}{\partial x_j}\right] - \overline{\rho u_i'' u_j''} \tag{6}$$

The anisotropic and the shear stress parts of the Reynolds stresses $\overline{\rho u_i'' u_j''} - \frac{2}{3}\rho k \delta_{ij}$ are included in the viscous fluxes. The stress tensor (6) contains a laminar and a turbulent part. For the Reynolds stresses the Boussinesq approximation is used

$$-\overline{\rho u_i'' u_j''} = \mu_T \left[\frac{\partial u_j}{\partial x_i} + \frac{\partial u_i}{\partial x_j} \right] - \frac{2}{3}\rho k \delta_{ij}. \quad (7)$$

where μ_T is a turbulent viscosity. The diffusion coefficients of the turbulence quantities are written as

$$\mu_k = \mu + \frac{\mu_T}{\sigma_k} \qquad \mu_\epsilon = \mu + \frac{\mu_T}{\sigma_\epsilon} \quad (8)$$

where σ_k and σ_ϵ are the appropriate Schmidt's numbers.

Turbulence Modeling

In the low-Reynolds number $k-\epsilon$ model, the solution is extended to the wall instead of using a wall-function approach [5]. The source term for Chien's model is given as

$$Q = \begin{pmatrix} P - \rho\tilde{\epsilon} - 2\mu\dfrac{k}{y_n^2} \\ c_1 \dfrac{\tilde{\epsilon}}{k} P - c_2 \dfrac{\rho\tilde{\epsilon}^2}{k} - 2\mu \dfrac{\tilde{\epsilon}}{y_n^2} e^{-y^+/2} \end{pmatrix} \quad (9)$$

where y_n is the normal distance from the wall, and y^+ is defined by

$$y^+ = y_n \frac{\rho u_\tau}{\mu_w} = y_n \frac{\sqrt{\rho \tau_w}}{\mu_w} \approx y_n \left[\frac{\rho |\nabla \times \vec{V}|}{\mu} \right]_w^{1/2} \quad (10)$$

In Chien's model $\tilde{\epsilon}$ is solved instead of ϵ. The variable $\tilde{\epsilon}$ is defined so that it obtains a zero value at the wall and the true dissipation can be expressed as $\epsilon = \tilde{\epsilon} + 2\frac{\mu}{\rho}\frac{k}{y_n^2}$. The production of turbulent kinetic energy is modelled using Eq. (7)

$$\begin{aligned} P &= -\overline{\rho u_i'' u_j''} \frac{\partial u_i}{\partial x_j} \\ &= \left[\mu_T \left(\frac{\partial u_j}{\partial x_i} + \frac{\partial u_i}{\partial x_j} \right) - \frac{2}{3}\delta_{ij}\rho k \right] \frac{\partial u_i}{\partial x_j} \\ &= \left[\mu_T \left(\frac{\partial u_j}{\partial x_i} + \frac{\partial u_i}{\partial x_j} \right) \right] \frac{\partial u_i}{\partial x_j} \end{aligned} \quad (11)$$

In the $k-\epsilon$ model the turbulent viscosity is calculated from

$$\mu_T = c_\mu \frac{\rho k^2}{\tilde{\epsilon}} \quad (12)$$

In order to avoid unphysical growth of the turbulent viscosity μ_T, e.g., near the stagnation point, the production of turbulent kinetic energy P is limited as suggested by Menter [6]

$$P = \min(P, 20\,\rho\tilde{\epsilon}) \quad (13)$$

According to the conducted tests [6], the maximum of the ratio $P/\rho\tilde{\epsilon}$ inside shear layers is about two and, therefore, this limit should not affect the well–behaving regions of the flow field. Only the problems encountered near the stagnation point will disappear.

The equations for k and ϵ contain empirical coefficients. In this study the following coefficients are applied

$$\begin{array}{lcllcl} c_1 &=& 1.44 & \sigma_k &=& 1.0 \\ c_2 &=& 1.92(1 - 0.22e^{-Re_T^2/36}) & \sigma_\epsilon &=& 1.3 \\ c_\mu &=& 0.09(1 - e^{-0.0115y^+}) & & & \end{array} \quad (14)$$

where the turbulence Reynold's number is defined as

$$Re_T = \frac{\rho k^2}{\mu\tilde{\epsilon}} \quad (15)$$

Numerical Methods

Basic Features

Since the flow is incompressible, the time derivative of density in Eq. (1) disappears. In a pseudocompressibility approach [3] this is replaced by an artificial time derivative of pressure, and the continuity equation $\nabla \cdot \vec{V} = 0$ is replaced by

$$\frac{1}{\beta^2}\frac{\partial P}{\partial \tau} + \nabla \cdot \vec{V} = 0 \quad (16)$$

where $P = p/\rho$. In the present approach the original conservative fluxes are retained, but utilizing the chain rule we obtain

$$\frac{\partial \rho}{\partial \tau} \approx \frac{\partial \rho}{\partial p}\frac{\partial p}{\partial \tau} = \frac{1}{\beta^2}\frac{\partial p}{\partial \tau} \quad (17)$$

i.e. the derivative $\partial\rho/\partial p$ is replaced by an artificial pseudocompressibility factor $1/\beta^2$ [7]. The following continuity equation is obtained

$$\frac{1}{\beta^2}\frac{\partial p}{\partial \tau} + \nabla \cdot \rho\vec{V} = 0 \quad (18)$$

The flow equations are solved using Roe's method [8], which was originally designed for compressible flow, but can be applied with the artificial compressibility concept. In the derivation of the Jacobian matrix of the flux-vector, the pseudolinearization $\partial\rho/\partial p = 1/\beta^2$ is applied for each density-derivative term. In the original method (16) a pressure-derivative term is added only into the continuity equation. In the present

way the characteristic speeds reduce to simple expressions of $\lambda_{1,2} = u \pm \beta$. With a compressible flow the corresponding speeds are $\lambda_{1,2} = u \pm c$, where c is the speed of sound. This makes the flux calculation straightforward and similar to the compressible formulae. The flux is calculated as

$$\hat{F} = T^{-1} F(TU) \tag{19}$$

where T is a rotation operator that transforms the dependent variables to a local coordinate system normal to the cell surface. In this way, only the Cartesian form F of the flux is needed. This is calculated from

$$\begin{aligned} F(U^l, U^r) &= \frac{1}{2}\left[F(U^l) + F(U^r)\right] \\ &- \frac{1}{2}\sum_{k=1}^{K} r^{(k)} |\lambda^{(k)}| \alpha^{(k)} \end{aligned} \tag{20}$$

where U^l and U^r are the solution vectors evaluated on the left and right sides of the cell surface, $r^{(k)}$ is the right eigenvector of the Jacobian matrix $A = \partial F/\partial U = R\Lambda R^{-1}$, the corresponding eigenvalue is $\lambda^{(k)}$, and $\alpha^{(k)}$ is the corresponding characteristic variable obtained from $R^{-1}\delta U$, where $\delta U = U^r - U^l$. A MUSCL-type approach has been adopted for the evaluation of U^l and U^r. In the evaluation of U^l and U^r, primary flow variables (p, u, v, w), and conservative turbulent variables (ρk, $\rho\epsilon$) are utilized. For the turbulence quantities, flux calculation utilizes second-order upwinding with a limiter of van Albada [9].

It should be noted that the flux calculation based on Eq. (20) can be interpreted as a central difference + a damping term. With an incompressible flow this damping term is based on β and is non-physical, but works properly. Since the damping term is not physically accurate, as is the case with the compressible flow assumption, it has been simplified and only significant terms are maintained.

Discretization

The quasi-steady approach and the time-accurate solution utilize the same basic steady-state algorithm. Since the differences between the two approaches are small, in the following the main features of the steady-state solution are firstly described. In the present solution, a finite-volume technique with a structured grid is applied. The flow equations have a discrete form

$$V_i \frac{dU_i}{d\tau} = \sum_{\text{faces}} -S(\hat{F} - \hat{F}_v) + V_i Q_i = R_i \tag{21}$$

where the sum is taken over the faces of the computational cell. The inviscid part of the flux is

$$\hat{F} = \begin{pmatrix} \rho\hat{U} \\ \rho u\hat{U} + n_x p \\ \rho v\hat{U} + n_y p \\ \rho w\hat{U} + n_z p \\ e\hat{U} + p\bar{U} \end{pmatrix} \tag{22}$$

Here $n_x\vec{i} + n_y\vec{j} + n_z\vec{k}$ is the unit normal vector of the cell face, $\bar{U} = n_x u + n_y v + n_z w$ is the velocity component normal to a stationary cell surface, and $\hat{U}$ is the convective velocity relative to the moving cell surface. The same flux formula is applied in the case of the time-accurate solution. In both cases the viscous fluxes are evaluated using a thin-layer approximation. The thin-layer model is activated in all coordinate directions.

Eq. (21) is integrated in time implicitly by applying the $DDADI$-factorization [10]. This is based on the approximate factorization and on the splitting of the Jacobians of the flux terms. The resulting implicit stage consists of a backward and forward sweep in every coordinate direction. The boundary conditions are treated explicitly, and a spatially varying time step is utilized. Hence, the integration is not accurate in time, but provides an iterative way to approach the steady-state. In order to further accelerate the convergence, multigrid cycling is used. The method of Jameson [11] with a simple V-cycle has been adopted. When the multigrid is activated, turbulence is not evaluated on the coarse levels. Instead, the turbulent viscosities are transformed onto the coarse grid levels, as are the other flow variables. This treatment is essential when the $k-\epsilon$-model is used, and it may also improve the stability with the algebraic model. More details of the solution algorithm are given in [4] and [12].

The time-accurate integration shares the same basic features described above, but now the pseudo time-integration is performed inside a physical time step and a true time derivative is added on the right-hand side of Eq. (21). A three-level fully implicit scheme is applied for the time-integration [13]. Then the residual R_i defined by the right-hand side of Eq. (21) is discretized in time as

$$\begin{aligned} R_i = &- V_i \frac{3U^{n+1} - 4U^n + U^{n-1}}{2\Delta t} \\ &- \sum_{\text{faces}} S(\hat{F}^{n+1} - \hat{F}_v^{n+1}) + V_i Q_i^{n+1} \end{aligned} \tag{23}$$

Here n indicates the time level and Δt is a physical time step. From Eq. (23) it is seen that the time-derivative term is treated as a source term. It should

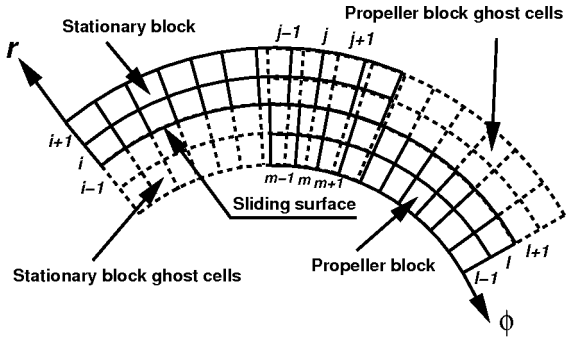

Figure 1: Interface between a moving block and a stationary block.

be noted that the time-derivative term replaces the additional source terms caused by the rotation and here Q only stands for the sources in the turbulence equations (9).

In the time-accurate case a kind of steady-state integration inside the true time step is performed using the solution methods described above. The left-hand side of Eq. (21) is utilized in the iteration exactly in the same way as in the steady-state calculation. The iteration converges as the residual of Eq. (23) approaches zero. During the solution the grid block describing the impeller rotates and a new position as well as the geometrical properties including the new rotational speeds are calculated as the calculation proceeds to the next time level. The impeller is connected to the rest of the domain using a sliding mesh technique. As a result the grid lines between the impeller blocks and the stator are discontinuous. A mass conserving interpolation is made between the connecting blocks at every time step [14]. This is discussed in the next section.

The flow solver utilizes a multiblock grid. The boundary conditions between the blocks are treated explicitly and only on the highest grid level. In order to decrease computational times the code is parallelized. The parallelization is done over the blocks. The details concerning the parallelization can be found from Ref. [15].

Sliding Mesh Model

The sliding mesh technique is ideally suited for problems involving rotor/stator interactions, e.g. propeller/ship hull geometry. In the sliding mesh technique two grids are employed: one for the stationary components and another for the propeller. The propeller grid moves with respect to the stationary grid along a sliding surface. Fig. 1 illustrates the interface between a propeller block and a stationary block.

Since the grid lines across the sliding surface are not continuous, the information transfer across the surface has to be done using interpolation. A conservative interpolation can be evaluated discretely as follows: Let C_j be the discrete flux in the propeller block to be interpolated at a particular ϕ position from the discrete flux in the stationary block. A piecewise constant projection of C from one grid on to the other is [14]

$$C_j = \sum_m C_m N_j^m$$

where

$$N_j^m = \begin{cases} 0, \text{ if } \phi_{m+1/2} < \phi_{j-1/2} \\ 0, \text{ if } \phi_{m-1/2} > \phi_{j+1/2} \\ \dfrac{1}{\Delta\phi_j} \displaystyle\int_{\max(\phi_{m-1/2},\phi_{j-1/2})}^{\min(\phi_{m+1/2},\phi_{j+1/2})} d\phi, \text{otherwise} \end{cases}$$

The N_j^m represent the relative area (angle) of overlap of cell m onto the cell j, ($0 \leq N_j^m \leq 1$). The discrete flux balance is maintained as

$$\sum_j C_j \Delta\phi_j = \sum_m C_m \Delta\phi_m$$

since $\sum_j N_j^m \Delta\phi_j = \Delta\phi_m = \phi_{m+1/2} - \phi_{m-1/2}$.

In the flow solver used in this study, it is required that at one time step (e.g. $t = 0$) the surface grids on the opposite sides of the sliding surface match each other. This means that the grid point clustering in the circumferential direction must be the same on both grids. The information transfer across the sliding surface is handled in two phases. In the first phase, the values in the ghost cells are updated by assuming a zero rotation angle. The values in the ghost cells of the moving block are copied from the corresponding stationary block cells, and the values in the stationary block ghost cells are copied from the appropriate moving grid cells. In the second phase, the ghost cell values are rotated according to the rotation angle. In this phase the interpolation weights N_j^m are utilized.

Assuming N computational cells in the circumferential direction, we get $(N+2)\times(N+2)$ interpolation weight matrix. The "+2"s represent the first ghost cells at the ends of the circular arc. These ghost cells are not shown in Fig. 1. The weight matrix is valid for all the circumferential cell rows, so it needs to be computed only once for each sliding patch.

PROPELLER IN A UNIFORM FLOW

Geometry and Meshing

The propeller selected for the RANS calculations is a 0.219 m diameter, four-bladed propeller of the BB-series. Measurements from open water tests performed at MARIN for the BB-series are found in [16].

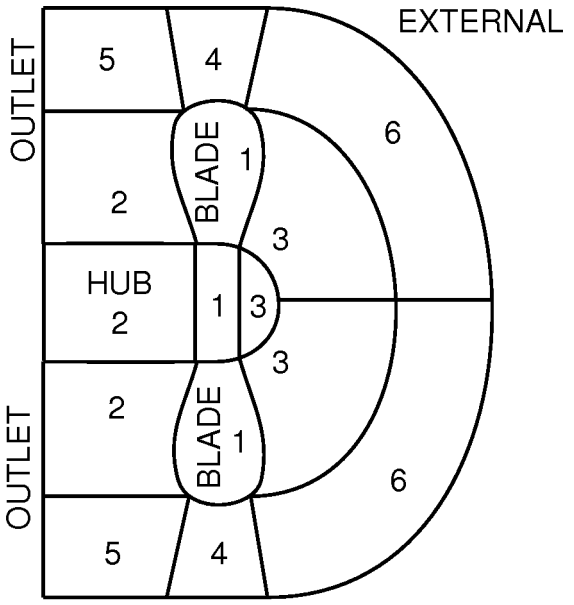

Figure 2: Position of the grid blocks and boundary conditions for the propeller.

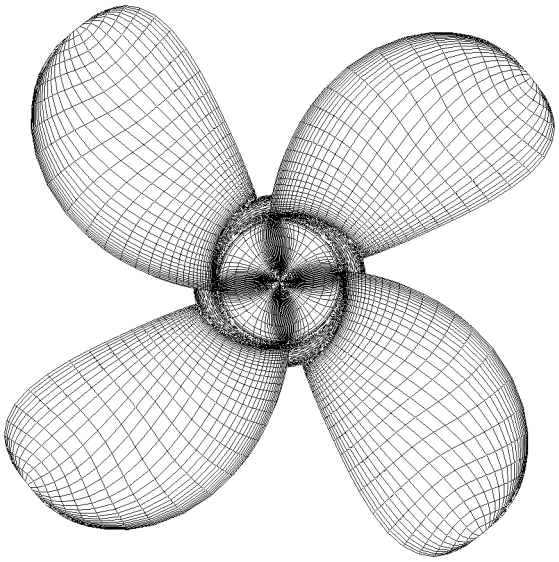

Figure 3: Surface grid of the propeller. Every other grid line is drawn.

Model tests have also been conducted at VTT. The Troost BB propeller in the VTT open water tests had a modified hub, i.e. the hub diameter ratio (about 0.23) was larger than that of the standard BB propeller and the coning angle was different. The same hub was also used in the Azipod tests made at VTT. The calculations presented in this paper correspond to the VTT geometry with an advance ratio $J = 0.8$, and Reynolds number $Re = 4 \times 10^5$.

For the RANS calculation only the space between two contiguous propeller blades was modelled to take full advantage of the periodicity of the flow and geometry. The grid consists of six blocks, and the topology is schematically shown in Fig. 2. The grid has the inlet boundary modelled by a spherical sector located at three diameters from the propeller centre. The outlet boundary is a plane located at $x/D = -3.0$, i.e. three diameters downstream of the propeller plane. Both boundaries are connected to each other by an external boundary consisting in a cylindrical surface placed at $r/D = 3.0$, i.e. at three diameters from the propeller axis. The total number of cells is about 1,300,000. Fig. 3 shows the surface grid of the whole propeller. Fine grid spacings are used in the vicinity of the leading and trailing edges of the propeller blades in the chordwise direction, and near the blade tip and hub in the radial direction. The minimum grid spacing in the circumferential direction for the resolution of the boundary layer is 0.3×10^{-5} m. After computations the parameter y^+ was found to be lower than 0.6 along most of the blade. Only at the tip the mean value of y^+ is a little higher than one.

The hub and blade surfaces of the propeller are rotating solid walls. The lateral surfaces adjacent to the propeller blades have a cyclic boundary condition. Block boundaries, where two adjacent block surfaces are coincident, are defined as connectivities. Uniform and inviscid flow conditions are applied to the inlet and external boundary surfaces, and the streamwise gradients of the flow variables are set to zero at the outlet.

Results

The computations were performed on a SGI Origin 2000 machine. Three processors were used. The computation time was 45 seconds per iteration cycle. For the second and third grid levels the CPU times are 1/8 and 1/64 times those of the first grid level, respectively. A satisfactory convergence was obtained with a Courant number of 0.5 and two multigrid levels. The convergence histories of the overall lift and drag coefficients are presented in Figs. 4 and 5.

Differences less than 1.5 % in the calculated thrust and torque coefficients and about 1.5 % in efficiency are found relative to measurements from MARIN, where, in fact, the Reynolds number was five times higher than that in the simulation. If experimental values obtained at VTT are chosen as the reference, calculations over-predict the thrust and torque coefficients by 4.5 %. However, the error in efficiency is only about 0.2 %. The discrepancies in the experimental measurements can be attributed to the differ-

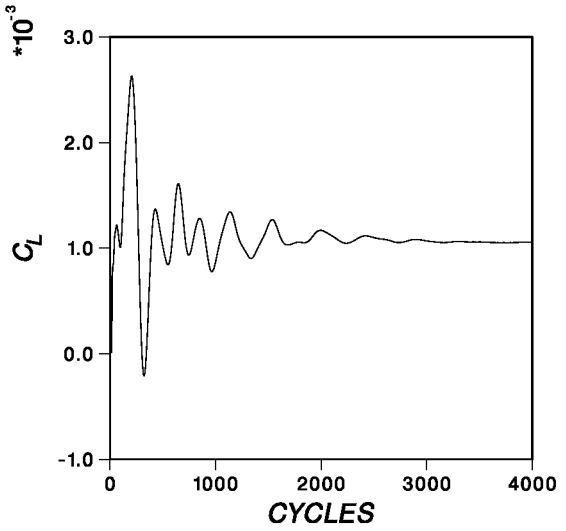

Figure 4: Convergence history of the lift coefficient for the propeller.

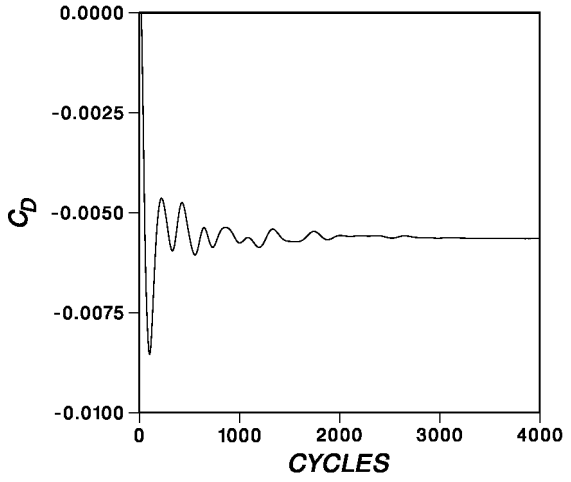

Figure 5: Convergence history of the drag coefficient for the propeller.

ences in both the Reynolds number used in the tests and the shape of the hub in the experimental models. In fact, the Reynolds number for which VTT tests were performed for this tentative Azipod version was close to 4×10^5 , which is small compared to 2×10^6 used in MARIN data. The experimental apparatus may also be responsible for part of the discrepancies, as it has been recognised in comparative tests performed at various towing tanks with identical propeller models.

When passing from the second grid level (coarse grid) to the first grid level (finest grid) the improvement of the efficiency prediction is about 4 % and that

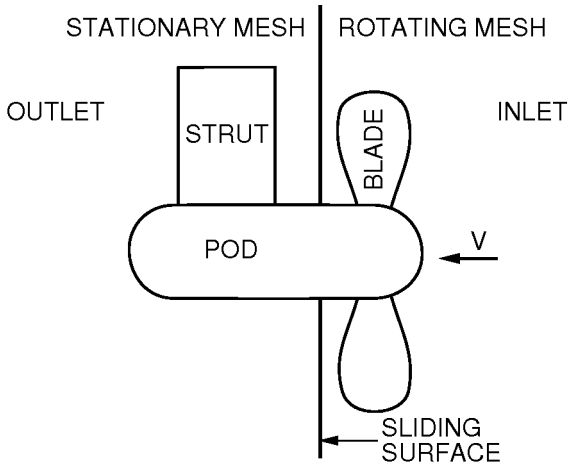

Figure 6: Geometry and boundary conditions for the tractor thruster.

of the thrust prediction about 2 %. This data will be useful when interpreting the correlation with experiments for the Azipod calculation.

THE TRACTOR THRUSTER

Geometry and Mesh

The thruster consists of the BB-series propeller mentioned in the preceeding section, a pod and a strut. A sketch of the geometry is shown in Fig. 6. The flow around the tractor thruster is no longer cyclic, as was for the case of the propeller alone. The strut breaks the symmetry. Consequently, periodic or cyclic boundary conditions cannot be applied anymore to reduce the computational domain, and the entire flow region must be meshed.

The grid consists of 17 blocks divided into two groups representing the space near and far away from the pod. The space near the pod extends from the pod to a distance of about one propeller radius. The space far away from the pod extends from the propeller radius to the outermost external boundary. The grid has a C-O topology in the axial-circumferential direction for the group of blocks far away from the pod, and a O-O topology for the blocks contiguous to the pod. The sliding surface is located between the propeller and the strut. The total number of cells is 814,080. The grid on the thruster surfaces is shown in Fig. 7. As it can be seen from the figure, the grid is more refined on the propeller blades than on the strut, since most of the comparisons presented in this paper relate to propeller forces.

The minimum grid spacing in the circumferential direction for the resolution of the boundary layer is about twice that of the grid of the computation for

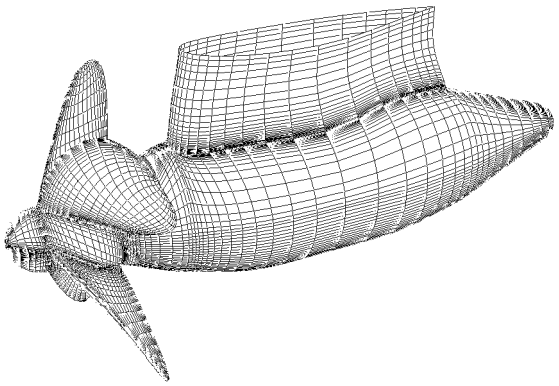

Figure 7: Grid on the thruster surface.

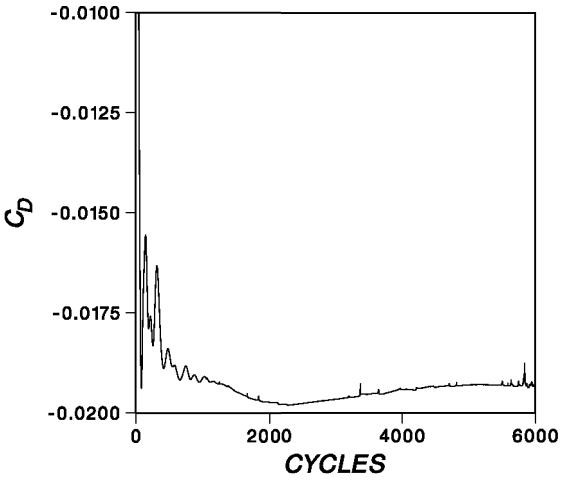

Figure 8: Convergence history of the drag coefficient for the tractor thruster. Quasi-steady simulation.

the propeller alone. This is enough to have the mean value of y^+ close to 1 at the 0.7 nondimensional radius of the propeller.

Convergence

Quasi-Steady Calculation

In these calculations the Courant number was 0.5, and the number of multigrid levels was two. The convergence history of the overall drag coefficient is presented in Fig. 8. The computation time with four processors was 19.8 seconds per iteration cycle.

Time-Accurate Calculation

The computation was started by taking as an initial guess the results obtained from the quasi-steady calculation. For the first grid level the Courant number

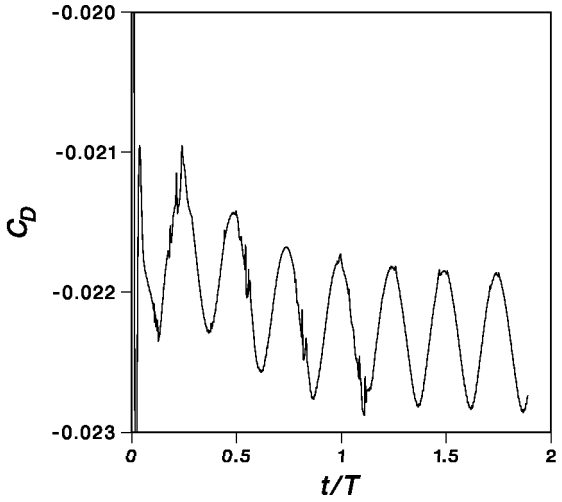

Figure 9: Convergence history of the drag coefficient for the tractor thruster. Time-accurate simulation.

was 5, the number of internal iterations per time step 50, and the time increment Δt corresponds to an angular step of 0.625°. It should be noted that the Courant number corresponds to the step-size of $\Delta\tau$ utilized inside the true time-step. In the time-accurate case $\Delta\tau$ can be larger than in the quasi-steady calculation. Slightly more than one thousand time steps were taken until a sufficiently stable periodic solution was established. The total computation time was almost 300 hours with four processors. The total CPU time required to obtain converged results for the forces and the moments is about 9 times that of the quasi-steady calculation.

The convergence history of the overall drag coefficient residuals for the first grid level is presented in Fig. 9. The corresponding history of the L_2-norm of the x-momentum residuals within five physical time steps is shown in Fig. 10.

In order to verify the precision of the time-accurate method, the simulation was performed on the second grid level using time-step sizes that correspond to angular steps of 0.625° and 1.25° This coarser grid has a number of cells equal to 1/8 of the first grid level (half of the cells in each one of the three block directions). The differences in the thrust and the torque coefficients between the calculations with different time steps are only about 1 %, which shows that the time-step size is adequate.

Analysis of Results

Quasi-Steady Calculation

After 3,000 iterations most of the forces, especially those on the propeller surfaces, have converged to one

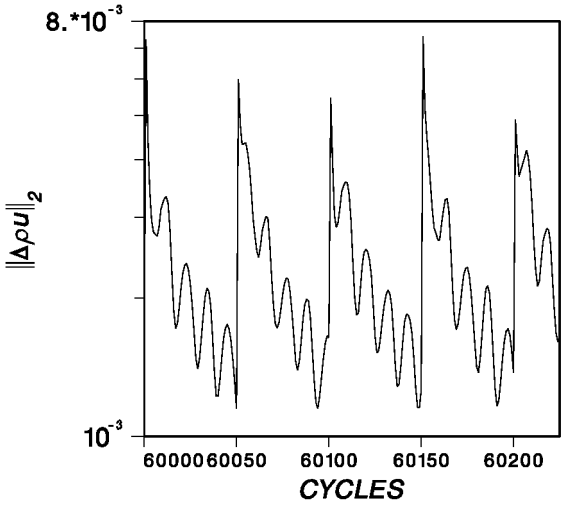

Figure 10: Convergence history of the L_2-norm of x-momentum residuals within five time steps.

percent accuracy. Differences from experimental values in thrust of 8.5 % and in efficiency of about 6.5 % appear. They can be attributed to several reasons:

1. The grid used for the Azipod calculations in the first level represents the propeller geometry with a little less precision than the second grid level of the propeller-alone grid. This means that the error could have been reduced by about 4-5 % in efficiency and 2-2.5 % in thrust, if a denser grid had been used. This error is estimated from the improvement of efficiency and thrust predictions when passing from the second grid level to the first one in the propeller-alone calculations.

2. The unsteadiness of the flow, not modelled in the quasi-steady calculation, reduces the mean thrust and torque coefficients due to the generation of the so-called shed vortices in the wake in addition to the free vortices always present in the steady-state results. The error can be estimated by comparing the quasi-steady results to the time-accurate results presented in the next section. It was found to be 0.9 % in the efficiency and 0.8 % in the thrust.

3. The tests were conducted with a plate located on the upper part of the Azipod. The calculations have been done without the plate. The strut has been progressively reduced in breadth at the plate location.

4. For the propeller-alone calculations the experimental thrust and torque coefficients from MARIN were about 4.5 % larger than those found at VTT. As mentioned before, the differences in the hub shape are not solely responsible for the large difference. Reynolds number effects and the experimental set up may well have some influence on it.

If a provision were made for the sources of the errors, the prediction of efficiency could be improved by about 4.9-5.9 % with a finer grid and a full unsteady calculation, and the remaining error of 0.6-1.6 % would be attributed to the deficiencies in the computational approach, e.g. limitations of the turbulence modelling, etc. As far as the thrust coefficient is concerned, the improvement would be 2.8-3.3 % relative to the VTT measurements. If the trend observed in the propeller-alone calculation for MARIN data is extrapolated to the Azipod calculation, the error when MARIN is chosen as a reference for the magnitude of the thrust could be further reduced by no more than 4.5%. This does not concern the efficiency, which would be more or less the same.

The calculated pressure distribution on the thruster surface is given in Figs. 11 and 12. The minimum pressures are located both on the leading edge of the propeller blades, close to the tip, and on the suction side of the strut. Tractor thrusters have the pod and strut located in the high-velocity region of the propeller wake. This means that higher viscous forces are expected on the pod and the strut surfaces than is the case with pushing thrusters. Non-symmetric struts and fins could be designed to alleviate to some extent this problem providing additional thrust, and they can also be shaped to reduce low pressure peaks.

Time-Accurate Calculation

After a rotation of 180° the propeller forces have converged to one percent accuracy. However, the overall forces require about two revolutions to converge. The strut forces converge before the pod ones, the latter being smaller. The mean propeller thrust and torque are reduced from the quasi-steady calculations by 0.8 and 1.7 %, respectively. The normalized fluctuations in time of propeller thrust, torque and efficiency are illustrated in Fig.13. The fluctuations in thrust (3.2 %) are higher than those of torque (2.8 %). This means that at the maxima of the thrust the instantaneous efficiency grows, and vice versa. The fluctuations of the efficiency are not as high as those of the thrust and the torque. A small shift between the thrust and the torque fluctuations is observed.

The forces on the strut exhibit less fluctuation amplitude than those on the propeller. Only the portion of the strut within the slipstream is affected by unsteady forces. This means that in the case of design-

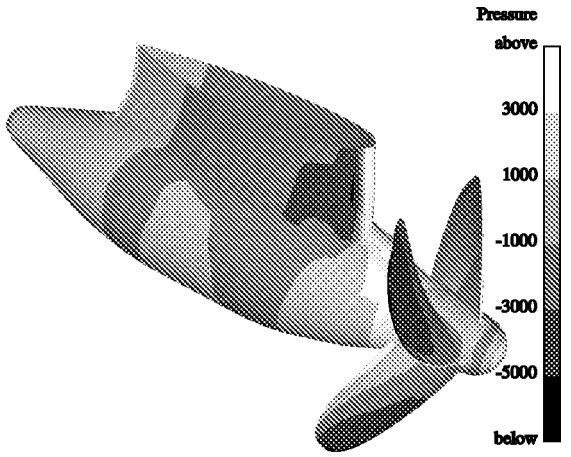

Figure 11: Distribution of pressure difference on the starboard side of the thruster surface. Quasi-steady simulation.

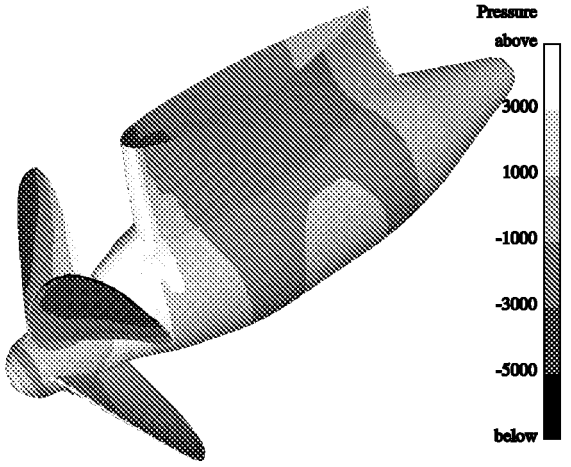

Figure 12: Distribution of pressure difference on the port side of the thruster surface. Quasi-steady simulation.

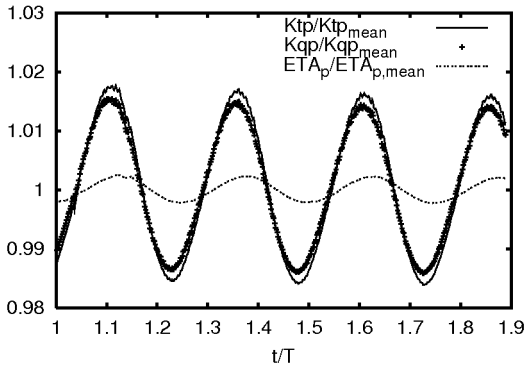

Figure 13: Fluctuations in time of propeller thrust, torque and efficiency.

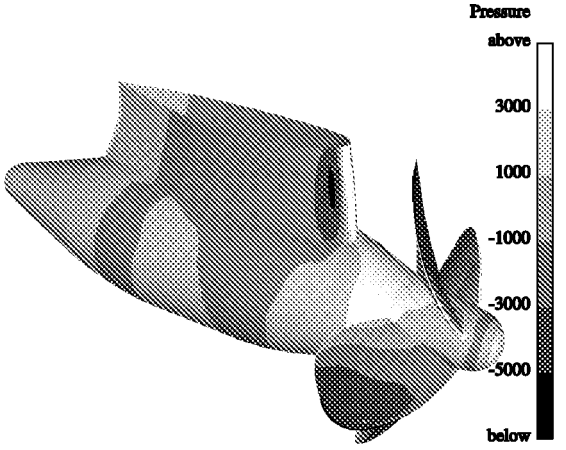

Figure 14: Distribution of pressure difference on the thruster for a reference angular position of the propeller. Time-accurate simulation.

ing non-symmetric struts the lack of symmetry in the strut geometry should be confined to the part washed by the propeller slipstream. The fluctuations on the hub are very small. The computation overpredicts both the thrusting force of the propeller and the drag force on the strut and pod. These effects tend to compensate each other, and an error of 5% in the total thrust of the unit results. The time-accurate computation was found to strongly improve the prediction of drag forces on the strut and pod.

The calculated pressure distribution on the thruster surface is given in Figs. 14-16 for different angular positions of the propeller (30° of angular increment) and in Fig. 17 for the propeller blades.

The minimum pressures are located both on the leading edge of the propeller blades, close to the tip, and on the suction side of the strut as it was in the case of the quasi-steady computation. However, the low pressure region on the suction side of the strut is not as extensive as before. This is probably a consequence of the higher loads present in the quasi-steady case due to the lack of the so-called shed vorticity found in unsteady potential-based methods. Fig. 17 reveals a non-uniform distribution of pressure near the leading edges of the blades, accompanied with low pressure peaks at the leading edges. Blade sections of NACA mean line $a = 0.8$ or modern blade sections, such as those designed with the Eppler method to delay cavitation inception, would display distinctly different pressure patterns in this area. It can be observed that the region of lowest pressure is larger for the blade located in front of the strut, as would be ex-

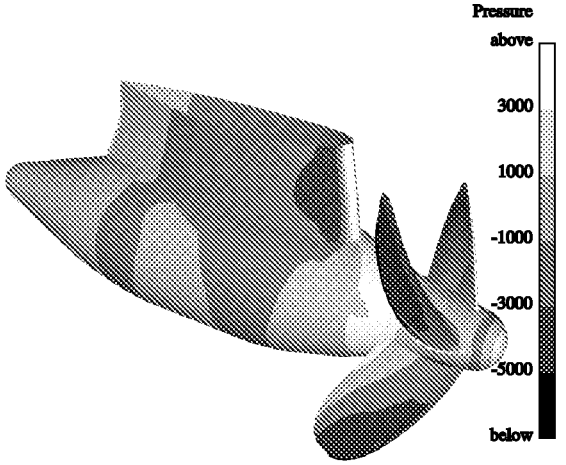

Figure 15: Distribution of pressure difference on the thruster for 30^o deviation from the reference angular position of the propeller. Time-accurate simulation.

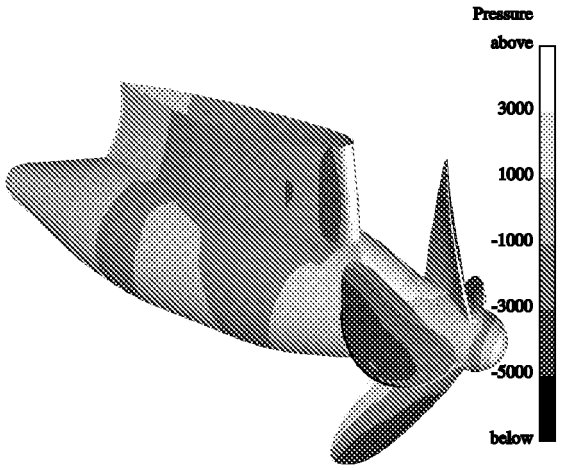

Figure 16: Distribution of pressure difference on the thruster for 60^o deviation from the reference angular position of the propeller. Time-accurate simulation.

pected due to the higher wake at the propeller plane.

CONCLUSIONS

In this paper the unsteady flow around a tractor thruster (pulling type) has been analysed by solving the RANS equations in combination with the sliding mesh technique.

First, the flow around a BB series propeller in steady flow has been computed using the $k - \epsilon$ turbulence model. The open water tests performed at MARIN and VTT have been used as validation data. Differences less than 1.5 % in the calculated thrust coefficient and about 1.5 % in the efficiency are found relative to measurements from MARIN. If experimental values obtained at VTT are chosen as a reference, calculations over-predict the thrust coefficient by 4.5 %. However, the error in efficiency is about 0.2 %. The discrepancies in the experimental measurements can be attributed to differences in both the Reynolds number used in the tests and the shape of the hub in the experimental models. The experimental apparatus may also be responsible for part of the discrepancies, as it has been recognised in comparative tests performed at various towing tanks with identical propeller models.

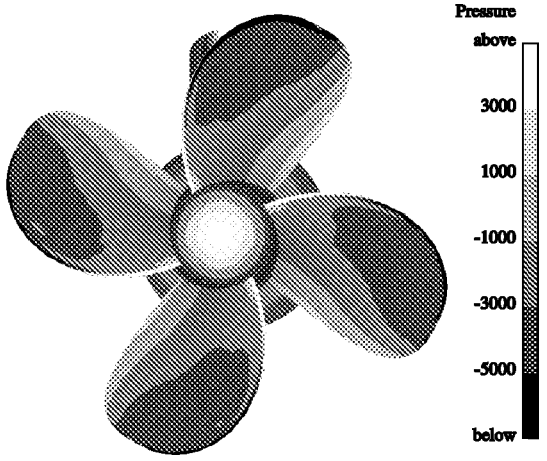

Figure 17: Distribution of pressure difference on the surface of the blades. Time-accurate simulation.

Secondly, simulations have been performed for the flow around the tractor thruster using the sliding-mesh technique. The computations have been performed in two different ways. For computations with circumferentially averaged flow through the sliding surface, larger differences from the experimental results appear in the computed thrust, torque and efficiency. This can mainly be attributed to several reasons: the mesh used for Azipod calculations is not as dense as that used in the propeller-alone computations; the unsteadiness of the flow tends to reduce the mean values of thrust and torque; uncertainty in the measurements at VTT and MARIN; and deficiencies of turbulence modelling.

Finally, a time-accurate computation has been conducted for the tractor thruster. Improvements in the prediction of the thrust and the torque coefficients by 0.8 and 1.7 % respectively, and of efficiency close to 1 % were achieved as compared to the quasi-steady calculation. Since the same relative coarse grid as in the quasi-steady case was utilized, the difference from the experimental data remains high. This is mainly due to the relatively coarse mesh used in the calculations. The time-accurate simulation strongly improves the

prediction of drag forces on the strut and pod relative to the time-averaged simulation. On the other hand the forces on the propeller are not significantly affected by the computational method. It should be noted that by utilizing parallelization more efficiently, the time-accurate computation could have been made in a dense grid with about 300 CPU hours.

Considering the two simulation approaches, the quasi-steady calculation allows the computer time to be reduced to about 1/10 compared to the latter. Its main merit consists of reducing the CPU time maintaining a full representation of the propeller geometry, i.e. without introducing simplified models for simulating the propeller action, such as actuator disk models or body force models like that presented in [17].

Tractor thrusters have the pod and strut located in the high-velocity region of the propeller wake. This means that higher viscous forces are expected on the pod and strut surfaces than is the case with pushing thrusters. Non-symmetric struts and fins could be designed to alleviate to some extent this problem providing additional thrust, and they can also be shaped to reduce the observed low pressure peak.

ACKNOWLEDGEMENTS

This research has been supported by the Technology Development Centre (TEKES). The Centre for Scientific Computing of Finland has provided its computing facilities. The validation presented in this paper has been possible thanks to the release of some experimental data by ABB-Azipod Ltd.

REFERENCES

1. Sanchez-Caja, A. "DTRC propeller 4119 calculations at VTT," 22nd ITTC Propulsion Committee Propeller RANS/Panel Method Workshop, ITTC, April 1998.

2. Siikonen, T., Hoffren, J. and Laine, S. "A multigrid *LU* factorization scheme for the thin-layer Navier–Stokes equations," Proceedings of the 17th ICAS Congress, Stockholm, Sept. 1990, pp. 2023–2034. ICAS Paper 90-6.10.3.

3. Chorin, A.J., "A numerical method for solving incompressible viscous flow problems," Journal of Computational Physics, Vol. 2, 1967, pp. 12–26.

4. Siikonen, T. and Pan, H. "Application of Roe's method for the simulation of viscous flow in turbomachinery," Proceedings of the First European Computational Fluid Dynamics Conference, Brussels, Elsevier Science Publishers B.V., Sept. 1992, pp. 635–641.

5. Chien, K.-Y., "Predictions of channel and boundary-layer flows with a low-Reynolds-number turbulence model," AIAA Journal, Vol. 20, No. 1, Jan 1982, pp. 33–38.

6. Menter, Florian R. "Zonal two equation $k-\omega$ turbulence models for aerodynamic flows," 24th AIAA Fluid Dynamics Conference, Orlando, Florida, Jul 1993. AIAA Paper 93-2906-CP.

7. Rahman, M.M., Rautaheimo, P. and Siikonen, T. "Numerical study of turbulent heat transfer from a confined impinging jet using a pseudo-compressibility method," Proceedings of the 2nd International Symposium on Turbulence, Heat and Mass Transfer, Delft, June 1997, pp. 511–520.

8. Roe, P.L., "Approximate Riemann solvers, parameter vectors, and difference schemes," Journal of Computational Physics, Vol. 43, 1981, pp. 357–372.

9. Van Albada, G.D., Van Leer, B. and Roberts, W.W., "A comparative study of computational methods in cosmic gas dynamics," Astronom. and Astrophys., Vol. 108, No. 76, 1982.

10. Lombard, C.K., Bardina, J., Venkatapathy, E. and Oliger, J. "Multi-dimensional formulation of CSCM — an upwind flux difference eigenvector split method for the compressible Navier–Stokes equations," 6th AIAA Computational Fluid Dynamics Conference, Danvers, Massachusetts, Jul 1983, pp. 649–664. AIAA Paper 83-1895-CP.

11. Jameson, A. and Yoon, S., "Multigrid solution of the Euler equations using implicit schemes," AIAA Journal, Vol. 24, No. 11, 1986.

12. Siikonen, T., "An application of Roe's flux-difference splitting for the $k-\epsilon$ turbulence model," International Journal for Numerical Methods in Fluids, Vol. 21, 1995, pp. 1017–1039.

13. Hoffren, J., Siikonen, T. and Laine, S., "Conservative multiblock Navier–Stokes solver for arbitrarily deforming geometries," Journal of Aircraft, Vol. 32, No. 6, 1995, pp. 1342–1350.

14. Rai, M.M., "A relaxation approach to patched-grid calculations with the euler equations," Journal of Computational Physics, No. 66, Dec 1986, pp. 99–131.

15. Rautaheimo, P., Salminen, E. and Siikonen, T. "Parallelization of a multi-block Navier–Stokes solver," Proceedings of the Third ECCOMAS Congress, Paris, John Wiley & Sons, Ltd., Sept. 1996.

16. Kuiper, G, "The wageningen propeller series," MARIN Publication, No. 92-001, May 1992.

17. Kerwin, J.E., Keenan, D.P., Black, S.D. and Diggs, J.G., "A coupled viscous/potential flow design method for wake-adapted, multi-stage, ducted propulsors using generalized geometry," SNAME Transactions, Vol. 102, 1994, pp. 23–56.

DISCUSSION

By M. Abdel-Maksoud

Thank you for the very interesting paper. Concerning figure 9, do you think that the unsteadiness of the maximum values of the drag coefficient is caused by numerical or physical reasons? Did you study the effect of the size of time step on the periodic variation of the drag coefficient?

Authors' reply

We are not quite sure about the nature of the small unsteadiness that appears in the convergence history of the overall drag coefficient. We have noticed that the unsteadiness is more pronounced for the smaller time steps in the calculation with the coarse grid. Hence, it is possible that the unsteadiness is caused by physical reasons, but is damped with larger time-steps. But it might also be caused by some convergence problems with shorter time-steps.

By H. Raven

For the thruster calculation it is stated that by using a finer grid the error would decrease by 4-5coarse/fine comparisons for open propellers. However, this would only be permitted if a precise indication of sign and magnitude of the error would be available. This would require solutions on at least 3 grids with sufficient refinement for the thruster case, followed by a check of the order of the error. Only under certain conditions the sign and magnitude of the error can then be estimated; otherwise it is an uncertainty; a fine grid then may just as well increase the deviation from experiment. In this paper, the error estimate seems to be based on just two grids, for a substantially different geometry and flow. This is obviously an unsafe procedure. Reference: 22nd ITTC Resistance Committee Report, Section 6

Authors' reply

In principle we agree that three grid levels are required for the error estimation. However, in this case the third grid level is prohibitively coarse. The error estimation is based on the fact that we have tested four different grids for open propellers having geometry and loading similar to that of the tractor thruster of this paper ranging from 900,000 to 1,300,000 cells. The differences in calculated performance coefficients for the grids have always been below one percent for the first grid level (fine grid). The improvement of results in performance coefficients when passing from the second grid level (coarse grid) to the first grid level has been for the different grids similar to that presented in this paper for the open propeller calculation, i.e. significant reduction of torque coefficient and, consequently, increase of efficiency.

The flow in the vicinity of an open propeller is not very different from that in the vicinity of a tractor thruster propeller. Tractor thrusters are characterised for having very small wake. Furthermore, in our calculation the portion of the grid surrounding the propeller is very close in shape for both the open propeller and tractor propeller. For these reasons we expect to correctly capture the trend in our extrapolation of the thruster propeller results to a finer grid, provided that the open propeller used for the extrapolation is the same as that of the tractor propeller and the sign of the corrections is maintained.